ACS NANO

www.acsnano.org

Article

Artificial Intelligence-Integrated Overcoupled Resonator for Multifunctional Pesticide Spectral Classification and Quantification

Dongxiao Li,[#] Ziwei Chen,[#] Xueyuan Wu, Tao Liu, Guozhi Zhang, Xiaojing Mu,* and Chengkuo Lee*

Cite This: *ACS Nano* 2026, 20, 7730−7742

Read Online

ACCESS | Metrics & More | Article Recommendations | Supporting Information

ABSTRACT: Pesticide residue detection plays a critical role in ensuring food safety, protecting human health, promoting environmental governance, and supporting sustainable agricultural practices. However, the growing diversity of pesticides, coupled with complex and overlapping spectral signatures and low residue concentrations, significantly limits the efficiency and applicability of conventional detection methods. Here, we present an overcoupled (OC) resonator platform integrated with artificial intelligence (AI) for multifunctional pesticide analysis. The OC resonator exhibits an ultrabroadband spectral response spanning 1650−750 cm^{-1}, representing up to a 1685-fold bandwidth enhancement compared with conventional narrowband resonators. Owing to this broadband characteristic, the OC resonator eliminates the need for resonance tuning when detecting different pesticide molecules. In addition, the OC resonator features high sensitivity and inherent immunity to Fano asymmetry, enabling identification and trace-level detection of multiple pesticide species. Experimental results demonstrate that the platform achieves a minimum limit of detection as low as 12.5 ng·μL^{-1} for pesticide molecules. To resolve the complexity and overlap in molecular spectral features, we incorporate AI algorithms for spectral classification, concentration prediction, and signal reconstruction, achieving 100% classification accuracy across complex mixtures. Furthermore, we validate the platform's real-world applicability by detecting pesticide residues on apple peels and in lake water, demonstrating excellent selectivity and strong interference suppression in complex backgrounds. This study not only expands the scope of OC resonator-based pesticide detection but also establishes a versatile framework for manipulating light−matter interactions, designing advanced plant sensors, and enabling ultratrace molecular diagnostics.

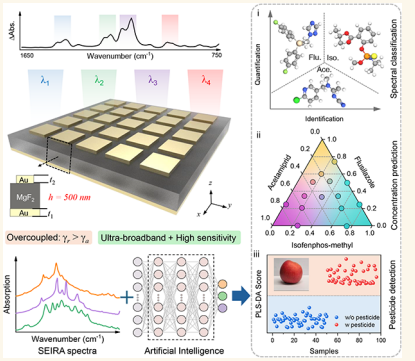

KEYWORDS: *metasurface, overcoupled resonator, artificial intelligence, pesticide residue detection, mid-infrared*

INTRODUCTION

In recent years, food safety has emerged as a pressing global public health concern, with pesticide residues being one of the most critical and widely scrutinized factors.[1] Although the extensive use of pesticides in agriculture has significantly improved crop yield and quality, their residual presence in fruits, vegetables, grains, water, and soil poses potential health risks through bioaccumulation in the food chain.[2] To safeguard public health, countries around the world have established stringent maximum residue limits and implemented corresponding evaluation and monitoring systems.[3−5] These increasing regulatory demands have, in turn, created a growing need for detection technologies that are not only highly sensitive and accurate but also capable of rapid, in-field operation under complex sample conditions. Conventional pesticide detection methods, such as gas chromatography (GC),[6] liquid chromatography (LC),[7] high-performance liquid chromatography (HPLC),[8] and enzyme-linked immunosorbent assays (ELISA),[9] offer excellent sensitivity and reliability for both qualitative and quantitative analysis. However, these techniques typically rely on expensive instrumentation, labor-intensive sample preparation, and trained personnel, making them unsuitable for rapid on-site detection or large-scale screening. Their limitations become particularly evident when dealing with complex real-world samples characterized by low analyte concentrations, coexisting multiple pesticide species, and interfering background signals. Therefore, there is an urgent need for a nondestructive, cost-effective, and rapidly deployable pesticide detection technology capable of operating under complex environmental conditions. Such a platform would be highly valuable for modern agriculture and the food industry in ensuring quality control and safety surveillance.

Mid-infrared (MIR) spectroscopy has emerged as a powerful technique for molecular identification and chemical analysis, owing to its ability to probe the intrinsic vibrational modes of molecules, providing rich information about molecular structures, chemical bonds, and functional groups.[10] In

Received: November 18, 2025
Revised: February 13, 2026
Accepted: February 17, 2026
Published: February 21, 2026

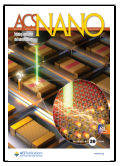

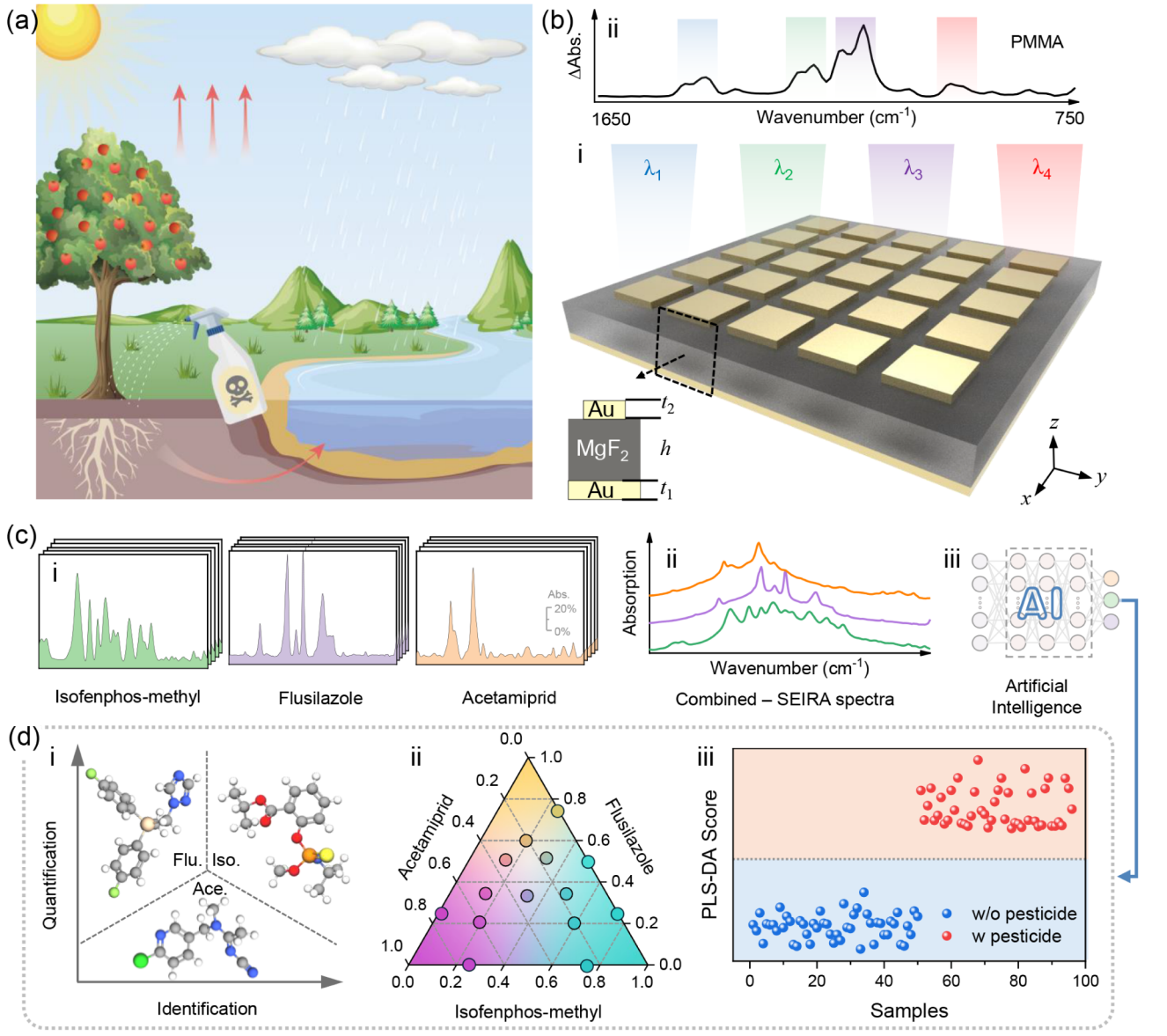

Figure 1. Schematic illustration of artificial intelligence (AI)-enhanced overcoupled (OC) resonator for pesticide sensing. a) Schematic representation of pesticide distribution in the environment. b) (i) Diagram of OC resonator featuring a broadband spectral response. (ii) Fingerprint vibrational spectrum of PMMA enhanced by the OC resonator. c) (i) Characteristic fingerprint spectra of three representative pesticide molecules (isofosmoticum-methyl, acetamiprid, and flusilazole). (ii) Mixed vibrational spectrum obtained by loading the three pesticides onto the OC resonator. (iii) Schematic of AI model. d) Integration of AI with spectra acquired from the OC resonator enables: (i) molecular classification, (ii) concentration prediction for mixed pesticides, and (iii) binary discrimination between contaminated and uncontaminated samples.

particular, surface-enhanced infrared absorption (SEIRA) spectroscopy enhances infrared absorption signals by generating strong localized electromagnetic fields on nanostructured surfaces,[11−15] enabling highly sensitive detection of trace molecules,[16−19] spectroscopic imaging,[20−22] and environmental monitoring.[23,24] Despite its potential, SEIRA platforms typically rely on narrowband resonant structures with high quality factors, which inherently conflict with the broadband and discrete nature of vibrational fingerprints commonly found in pesticide molecules. Narrowband resonators can only amplify signals within a limited spectral window, restricting the spectral information available and significantly impeding the identification of multiple components or the quantification of mixtures. Additionally, the uneven spacing of pesticide fingerprint peaks often lead to spectral detuning from the resonance, further reducing detection sensitivity. To address this, various strategies such as pixelated metasurfaces,[25−28] multimodal resonance,[29−31] two-dimensional material tuning,[32,33] and angular multiplexing[21,34] have been proposed to broaden the operational bandwidth. However, these methods are often hindered by structural complexity and fabrication challenges, which limit their scalability and practical applicability in real-world scenarios. Recently, overcoupled (OC) resonators has emerged as a promising alternative.[35−39] The OC resonator array can be understood as a type of engineered metasurface, where the periodic arrangement of nanoscale antennas enables precise control of light-matter interactions at the subwavelength scale. By engineering the radiation loss channels, an OC resonator achieves ultrabroadband spectral response, high sensitivity, and restored spectral symmetry, all within a single structural array.[36] These unique properties significantly enhance the adaptability and robustness of SEIRA

https://doi.org/10.1021/acsnano.5c20156
ACS Nano 2026, 20, 7730−7742

platforms for complex molecular fingerprinting. However, to date, no study has explored the application of OC resonators for multicomponent pesticide residue detection or complex mixture analysis. Their enhancement performance and recognition capabilities in real-world agricultural samples remain to be systematically validated.

As infrared sensing platforms evolve toward broadband and multitarget detection, the resulting high-dimensional, multifeature, and low signal-to-noise ratio (SNR) spectral data present significant challenges for traditional analytical methods. This is especially problematic in scenarios where multiple pesticide residues coexist, due to severe spectral overlaps and interference between molecular absorption peaks.[40] Under such conditions, conventional manual or rule-based analysis methods often fail to achieve accurate molecular identification and concentration quantification.[41] In this context, artificial Intelligence (AI) has emerged as a powerful tool to enhance the performance of SEIRA-based molecular recognition, owing to its capabilities in nonlinear modeling, pattern recognition, and complex data processing.[42−46] By applying AI algorithms for feature extraction, dimensionality reduction, and classification of SEIRA spectra, it becomes possible not only to distinguish overlapping spectral signatures of different molecules, but also to accurately model their concentration gradients.[19,41] Among various algorithms, principal component analysis (PCA) is widely used for feature compression and clustering; support vector machines (SVMs) demonstrate excellent classification performance under small sample conditions; and deep learning models such as multimodal deep neural network (MM-DNN) offer strong nonlinear regression capabilities. Integrating these algorithms with broadband SEIRA platforms opens new avenues for developing high-throughput, intelligent systems for real-world pesticide residue analysis, overcoming the limitations of traditional infrared molecular sensing.

Here, we present an AI-enhanced OC resonator featuring a broadband spectral response for rapid, efficient, and nondestructive identification of multiple pesticide molecules. Within the framework of temporal coupled-mode theory (TCMT), we systematically tuned the resonator from an undercoupled (UC) to an OC regime by engineering its radiative and intrinsic loss channels. This tuning strategy enables simultaneous enhancement of multiple fingerprints signals, broadens the spectral bandwidth, and remains immune to asymmetric Fano resonances, thereby overcoming the major limitations of conventional narrowband SEIRA platforms. Theoretical analysis indicates that the bandwidth of the OC resonator is enhanced by up to 1685-fold compared with traditional narrowband resonators. To experimentally validate this capability, poly(methyl methacrylate) (PMMA) is employed as a probe molecule, demonstrating pronounced spectral enhancement over the 1650−750 cm^{-1} range. Subsequently, we selected three representative pesticides (isofosmoticum-methyl, acetamiprid, and flusilazole) and prepared a series of samples with varying concentration gradients and mixture ratios. Their SEIRA spectra were collected and analyzed using machine learning techniques, including PCA, SVMs, and MM-DNN. The proposed platform achieves 100% classification accuracy for the selected pesticide mixtures and exhibits a minimum limit of detection as low as 12.5 $ng{\cdot}\mu L^{-1}$. Furthermore, we conducted spiked sample tests on apple peels and lake water to evaluate real-world applicability. Using partial least-squares discriminant analysis (PLS-DA), we successfully discriminated between pesticide-contaminated and uncontaminated samples. These results demonstrate that the AI-integrated OC platform offers superior performance in multicomponent pesticide detection and holds significant promise for applications in food safety monitoring, environmental pollution assessment, and agricultural residue management.

RESULTS AND DISCUSSION

Concept and Methodology of the Sensing Platform

The overall concept of the AI-enhanced OC pesticide detection platform developed in this study is illustrated in Figure 1. As shown in Figure 1a, ensuring both the quality and yield of agricultural products remains a core objective in modern agricultural practices. To enhance crop resistance and productivity, pesticides (insecticides, fungicides, and herbicides) are widely applied throughout crop cultivation and management.[47] However, statistical data reveal that less than 0.1% of the applied pesticide reaches its target pest.[48] The vast majority remains on the surface of crops, accumulates in soil and water, and eventually enters the food chain, posing potential threats to ecosystems and public health.[49] Therefore, there is an urgent need to develop a high-sensitivity, broadband, and portable sensing technology for rapid pesticide detection to support sustainable agriculture and food safety.

To address this need, we designed and fabricated an OC infrared resonator based on a metal−insulator−metal (MIM) architecture (Figure 1b-i). The structure consists of a bottom reflective metal layer, a middle dielectric spacer, and a top nanostructured antenna layer. Gold (Au) is used for both metal layers due to its favorable plasmonic properties, while magnesium fluoride (MgF_2), a low-loss dielectric in the infrared regime, serves as the spacer material. The bottom metal layer has a thickness of 100 nm, effectively blocking light transmission ($T = 0$). This allows the absorption spectrum to be simplified as $A = 1 - R$, enabling efficient operation of the platform in reflection mode. In the resonator design, we employed TCMT to precisely control the thickness of the MgF_2 layer and tailor the ratio between radiative and intrinsic loss rates, enabling the resonator to operate in OC regime. The detailed strategy for tailoring the OC conditions will be discussed in the next section. Under this regime, the resonator not only significantly enhances the interaction between incident infrared light and molecular vibrational modes, but also effectively suppresses the spectral asymmetry caused by Fano resonance. As shown in Figure 1b-ii, the extracted spectral line shapes become more symmetric and stable, while the sensitivity and robustness for detecting weak fingerprint peaks are also improved.

Building upon these advantages, we applied the OC platform to the detection of three representative pesticide molecules: isofosmoticum-methyl, acetamiprid, and flusilazole. As shown in Figure 1c-i, all three molecules exhibit multiple characteristic absorption peaks in the mid-infrared fingerprint region, with substantial spectral overlap among them. This overlap severely limits the effectiveness of conventional narrowband plasmonic resonators in distinguishing between such chemically similar compounds. To address this challenge, a broadband-enhanced plasmonic structure is required for the simultaneous detection of multiple absorption peaks. The proposed OC resonator fulfills this requirement by significantly enhancing the response intensity across a wide spectral range, enabling comprehensive

https://doi.org/10.1021/acsnano.5c20156
ACS Nano 2026, 20, 7730−7742

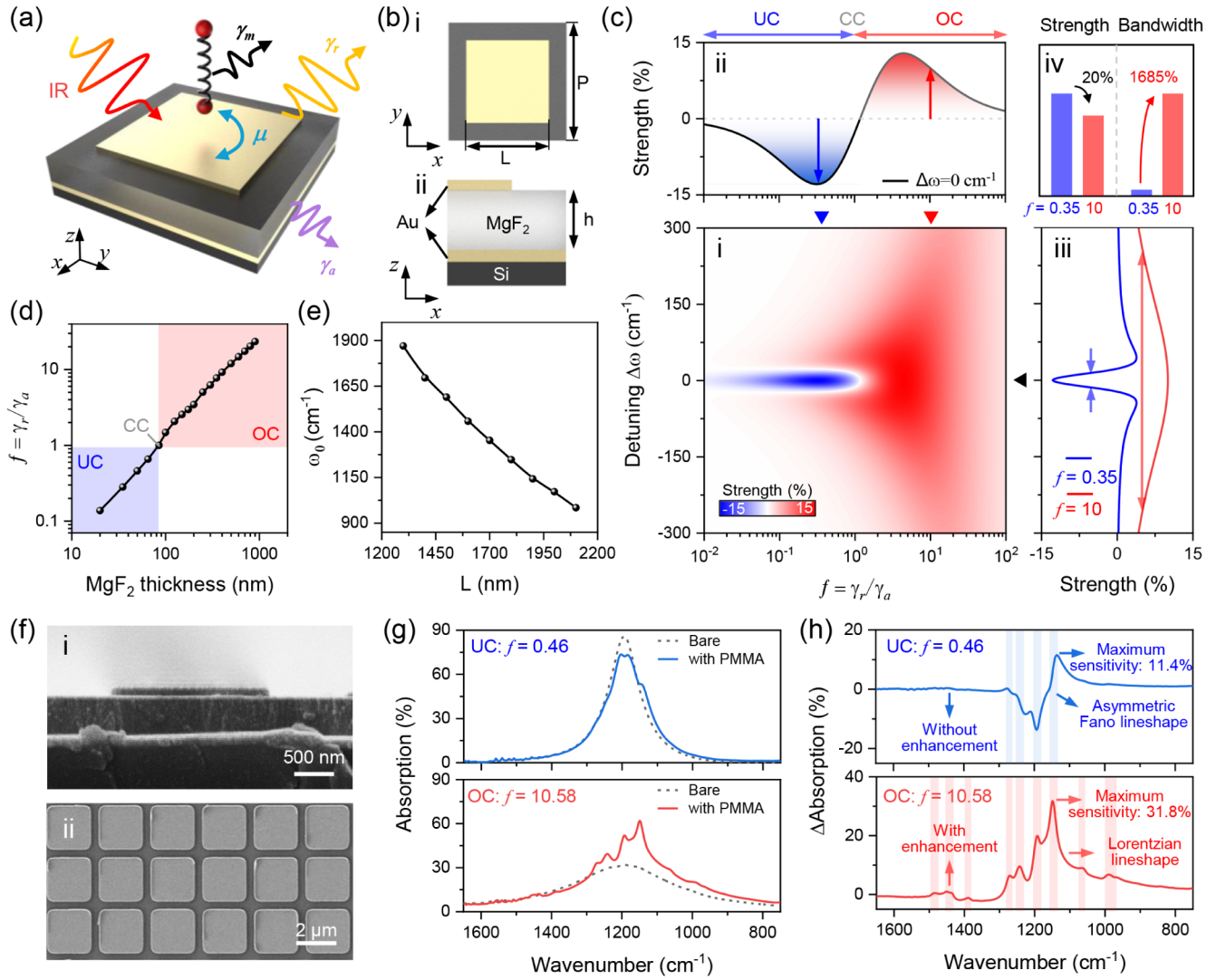

Figure 2. Design and sensing performance of OC resonator. a) Schematic of a molecule-coupled metal−insulator−metal (MIM) resonator. Here, γ_r and γ_a represent the radiative and intrinsic absorptive losses of MIM resonator, respectively. γ_m denotes the molecular absorptive loss, and μ is the coupling strength between the molecule and the MIM resonator. b) (i) Top view of MIM resonator unit cell. P indicates periodicity, and L is the side length of the square nanoantenna. (ii) Cross sectional view of the unit cell. The bottom and top metallic layers are gold, each 100 nm thick. The insulating layer is MgF_2 with a thickness of h, and the resonator is fabricated on a silicon substrate. c) (i) The sensitivity map was calculated using temporal coupled-mode theory (TCMT). (ii) Sensitivity as a function of the loss ratio ($f = \gamma_r/\gamma_a$) under spectral matching conditions ($\Delta\omega$ = 0 cm^{-1}). (iii) Sensitivity as a function of spectral detuning under f = 0.35 (blue) and f = 10 (red). (iv) Bar chart comparing sensitivity and spectral bandwidth. f) SEM images of OC resonator: (i) cross-sectional view and (ii) top view. g) Absorption spectra of the undercoupled (UC, blue) and OC (red) resonators after PMMA loading. Dashed curves indicate the absorption spectra without PMMA loading. h) SEIRA enhancement spectra extracted from the absorption spectra in (g).

detection of multiple fingerprint features within complex pesticide mixtures. As shown in Figure 1c-ii, the SEIRA spectra of mixed pesticide samples exhibit significant complexity, with extensive peak overlap and line shape variation. These spectral features reflect the chemical diversity and interactions among the components, which pose major challenges for molecular identification and quantification using conventional manual or rule-based spectral decomposition approaches.

To overcome this bottleneck, we incorporated AI algorithms to model and interpret the SEIRA spectra (Figure 1c-iii). As shown in Figure 1d-i, the AI-based classification model successfully distinguished among the three pesticide species with high accuracy. Furthermore, we prepared 14 mixtures of pesticides with varying ratios and applied MM-DNN to reconstruct their constituent profiles. The results are visualized in a ternary plot (Figure 1d-ii), where each point represents a single mixture, and its position indicates the predicted relative concentrations. To further evaluate the platform's real-world applicability, we prepared simulated samples with and without pesticide residues and employed a PLS-DA model for classification. As shown in Figure 1d-iii, the AI-enhanced platform clearly discriminates between pesticide-contaminated (red points) and uncontaminated (blue points) samples, with a well-defined classification boundary and high accuracy. These results demonstrate the strong practicality and generalizability of the OC-AI platform, highlighting its promise for rapid food safety screening and agricultural contamination monitoring.

https://doi.org/10.1021/acsnano.5c20156
ACS Nano 2026, 20, 7730−7742

Design and Sensing Performance of the Overcoupled Resonator

To enable simultaneous detection of multiple vibrational fingerprints of pesticide molecules, we designed an infrared resonator with ultrabroadband spectral response (Figure 2a). The resonator adopts classical MIM architecture.[50,51] This design is selected for its high degree of flexibility in tuning radiative and intrinsic loss parameters, which is essential for engineering adjustable coupling regimes.[35,38] The unit cell structure of the MIM resonator is illustrated in Figure 2b, where P denotes periodicity, L is the length of the top square nanoantenna, and h represents the thickness of the intermediate MgF_2 dielectric layer. To guide the device design, we employed TCMT to construct a spectral dispersion model for the absorption profile of the resonator under molecular coupling conditions (see Supporting Information Section S1 for detailed derivation).[35,52]

$$A = 1 - \left| \frac{\kappa^2}{j(\omega - \omega_0) + (\gamma_r + \gamma_a) + \frac{\mu^2}{j(\omega - \omega_m) + \gamma_m}} - 1 \right|^2 \quad (1)$$

In this model, ω_0 represents the intrinsic resonant frequency of the resonator, while ω_m corresponds to the characteristic vibrational frequency of the target molecule. γ_r and γ_a denote the radiative and intrinsic (absorptive) losses of the resonator, respectively, and γ_m represents the absorption loss contributed by the molecule. κ is the coupling coefficient between the incident light and the resonator ($\kappa = (2\gamma_r)^{1/2}$), and μ describes the coupling strength between the resonator and the molecule. The SEIRA absorption spectrum (ΔA) is defined as the difference between the absorption spectra of the molecule-loaded and molecule-unloaded states, expressed as

$$\Delta A = A - A|_{\mu=0} \quad (2)$$

We define the value of ΔA at the molecular absorption frequency ω_m as the sensitivity of the structure to the target molecule.

Building on this foundation, we further investigated the relationship between the sensitivity of the MIM resonator and key system parameters, including spectral detuning ($\Delta\omega = \omega_0 - \omega_m$) and the coupling ratio ($f = \gamma_r/\gamma_a$). A two-dimensional sensitivity map was generated to visualize the response characteristics (Figure 2c-i. The results reveal that the blue region, primarily located in the UC regime, corresponds to negative amplitude modulation, whereas the red region, concentrated in the OC regime, exhibits enhanced positive amplitude modulation (Figure 2c-ii). Because the critically coupled (CC) condition lies at the transition between positive and negative modulation, its sensitivity is lower than that of both the UC and OC regimes (spectral details are provided in Figure S1 of Supporting Information). Therefore, in this work, we focus on comparing the sensitivity performance of the UC and OC regimes. To further analyze the bandwidth performance, we selected two representative devices for comparison: one operating in the UC regime with $f = 0.35$ (blue arrow), and the other in the OC regime with $f = 10$ (red arrow). The corresponding sensitivity curves as a function of spectral detuning are shown in Figure 2c-iii (see Supporting Information Figure S2 for spectral details). Notably, the OC-mode resonator not only offers significant molecular enhancement but also achieves a substantially broader detuning range. It is worth mentioning that we did not choose $f = 5$, which yields the highest sensitivity in the OC mode, but instead selected $f = 10$ for further validation. Although the peak sensitivity at $f = 10$ is approximately 20% lower than that at $f = 0.35$ and $f = 5$, the bandwidth is improved by roughly 1685% and 26% (Figure S3, Supporting Information), respectively. We believe that this trade-off of moderately sacrificing sensitivity to achieve a substantial bandwidth gain is highly advantageous for mixed-molecule sensing applications.

Subsequently, we performed numerical simulations to further verify the tunability of the coupling state by varying device parameters (see Materials and Methods for simulation details). The results show that adjusting the thickness of the MgF_2 dielectric layer significantly modifies the radiative and absorptive loss rates of the resonator, thereby tuning the coupling ratio f (Figure S4, Supporting Information). When the dielectric thickness is less than 85 nm, $f < 1$, indicating UC regime; in contrast, when the thickness exceeds 85 nm, $f > 1$, placing the system in the OC regime (Figure 2d). Based on this, we selected a structure with a 500 nm-thick dielectric layer for subsequent experiments, corresponding to $f = 10$. Next, we evaluated the frequency tunability of the structure (Figure S5, Supporting Information). The results show that adjusting the length L of the square antenna can effectively tune the resonance frequency (Figure 2e).

In the experimental validation, we fabricated both UC and OC MIM resonators using standard micro- and nanofabrication processes (see Materials and Methods for details). Figure 2f presents the cross-sectional and top-view scanning electron microscopy (SEM) images of OC device, with a dielectric layer thickness of 500 nm, nanoantenna length of 2 μm, and unit cell period of 2.5 μm. The corresponding SEM images of the UC device are provided in Figure S6. To enable a fair comparison, the UC structure was spectrally tuned to match the resonance frequency of the OC device. Next, we use TCMT to fit the measured absorption spectra (Figure S7, Supporting Information). The fitting results show that the loss rate $f = 0.46$ for UC and $f = 10.58$ for OC devices. To assess molecular detection performance, we used a PMMA thin film as the probe molecule for SEIRA spectroscopy. Figure 2g shows the SEIRA absorption spectra in UC (blue) and OC (red) modes after PMMA loading. The corresponding dashed curves represent the absorption spectra without PMMA loading. The extracted differential absorption spectra are shown in Figure 2h. It is evident that the OC resonator enhances more molecular vibration modes, demonstrating superior fingerprint recognition capability compared to the UC mode. More importantly, the OC device effectively suppresses the spectral asymmetry typically induced by Fano resonance, resulting in a symmetric Lorentzian line shape in the SEIRA spectra. This symmetry greatly simplifies spectral postprocessing by eliminating the need for secondary baseline correction, an especially advantageous feature when analyzing chemically complex pesticide mixtures. In such cases, conventional narrowband resonators often suffer from Fano-induced distortion, which impairs accurate interpretation of overlapping spectral features.[53] In contrast, the stable spectral response of the OC structure provides a robust and reliable foundation for decoding multipeak molecular information in complex systems.

https://doi.org/10.1021/acsnano.5c20156
ACS Nano 2026, 20, 7730−7742

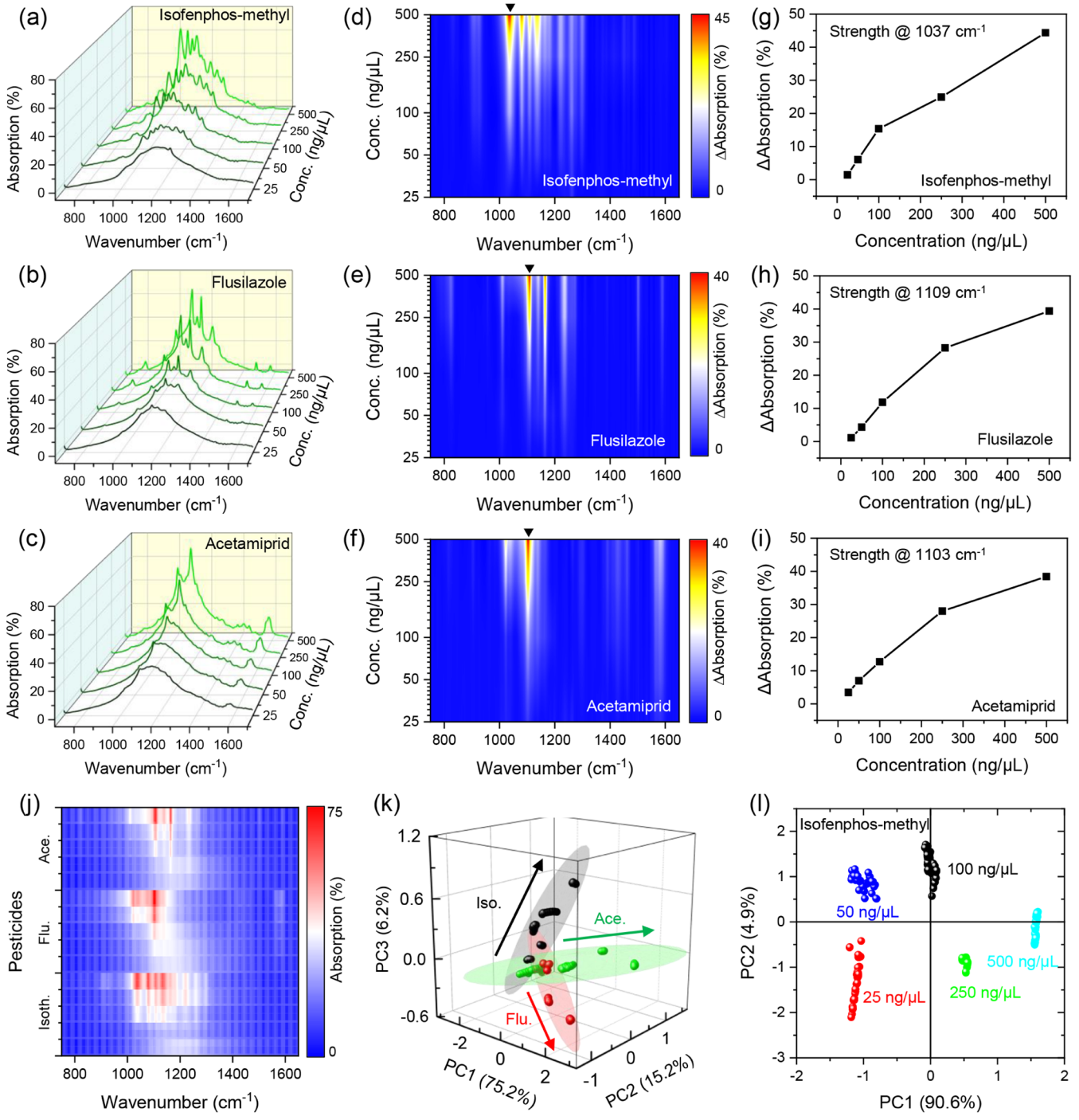

Figure 3. Quantitative detection and classification of pesticides using OC resonator. a–c) Absorption spectra of OC resonator loaded with isofosmoticum-methyl, acetamiprid, and flusilazole at concentrations ranging from 25 ng/μL to 500 ng/μL. d–f) Corresponding SEIRA enhancement spectra extracted from (a–c), showing intensity variations as a function of concentration. g–i) Intensity of representative vibrational peaks extracted from (d–f), plotted against analyte concentration. j) Absorption spectra collected from the OC resonator loaded with different pesticide types and concentrations. Each configuration contains 50 spectra. k) Principal component analysis (PCA) applied to the spectra in (j), visualized using the first three principal components in a 3D feature space. l) PCA of isofosmoticum-methyl spectra at different concentrations, visualized in a 2D feature space to illustrate concentration-dependent distribution.

Multi-Fingerprint Enhancement and Quantitative Detection of Pesticides

Pesticide molecules typically exhibit rich and distinct mid-infrared vibrational fingerprints. As shown in Figure 1c-i, even a single pesticide presents multiple characteristic peaks, while different pesticides display highly complex and overlapping vibrational features. Conventional narrowband metasurfaces have difficulty identifying and distinguishing such signals. In the previous section, we systematically demonstrated that OC resonator platform possesses several unique advantages (ultrabroadband response, high sensitivity, and intrinsic immunity to Fano-resonance-induced line-shape asymmetry) making it an ideal platform for multifingerprint enhancement and detection. In this section, we further validate the OC

https://doi.org/10.1021/acsnano.5c20156
ACS Nano 2026, 20, 7730–7742

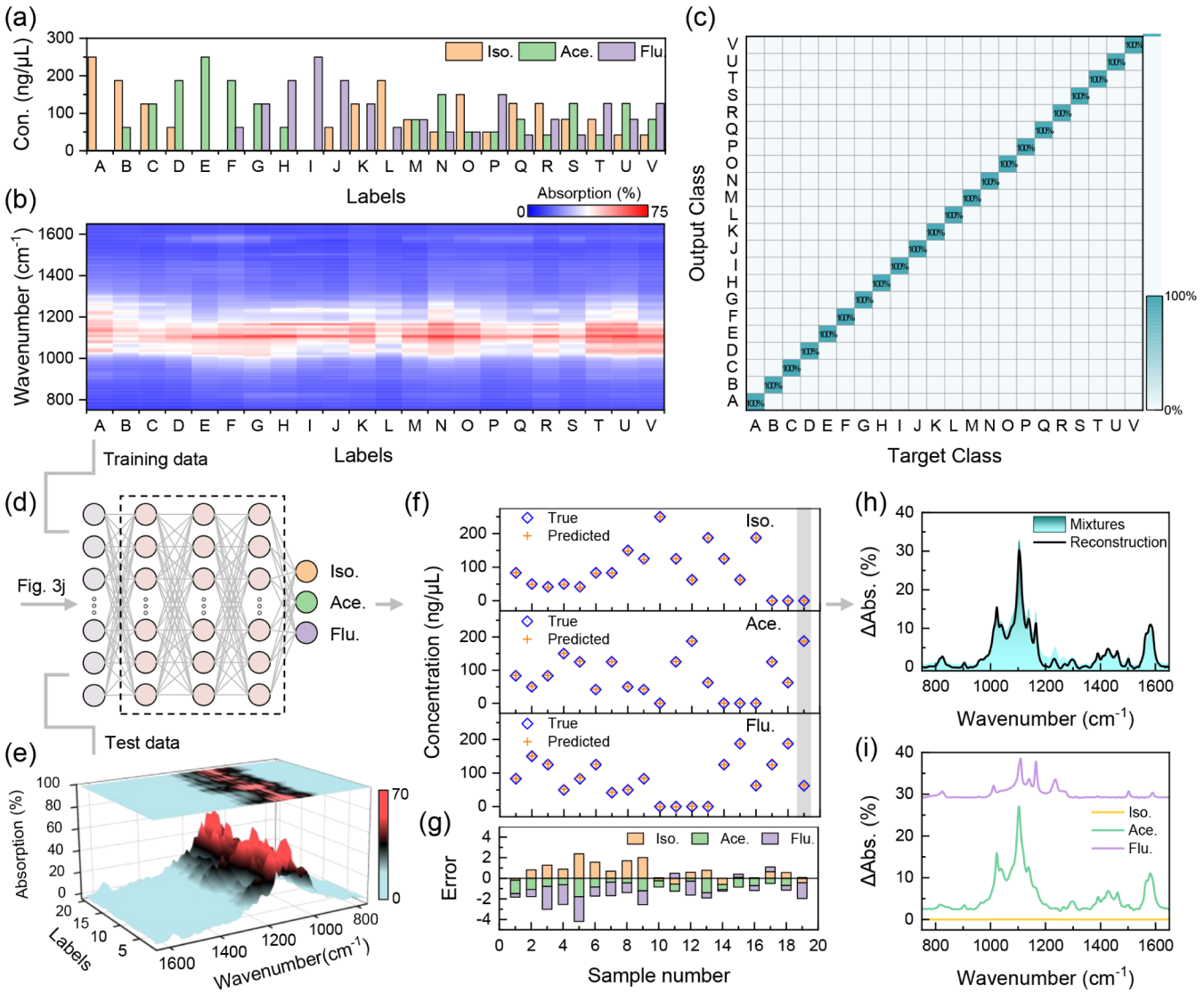

Figure 4. AI-enhanced OC resonator for mixed pesticide identification and concentration prediction. a) Bar chart showing the titrated concentration combinations of three pesticide molecules. b) Collected absorption spectra of mixtures with varying pesticide ratios. c) Classification of spectra from (b) using a support vector machine (SVM). The confusion matrix demonstrates 100% accuracy in mixed pesticide identification. d) Schematic of the multimodal deep neural network (MM-DNN) model used for concentration prediction. e) A new set of mixed spectra was measured and used as the test set for concentration prediction. f) Comparison of predicted and actual concentrations. g) Bar chart of prediction errors. h) Spectral reconstruction of sample 19: cyan shading indicates the differential spectrum of the mixture; black curve represents the reconstructed mixed spectrum. (i) Decomposition of the reconstructed spectrum in (h) into individual component spectra corresponding to different pesticides.

resonator's performance and versatility in enhancing and detecting multiple vibrational peaks of pesticide molecules. We highlight its potential in lowering the limit of detection (LoD), improving signal quality, and enabling rapid fingerprint extraction.

Three representative pesticides (isofosmoticum-methyl, acetamiprid, and flusilazole) widely used in agriculture were selected as the target analytes to evaluate the OC resonator's capabilities in complex multicomponent systems. Specifically, we deposited pesticides at different concentrations (ranging from 25 ng·μL^{-1} to 500 ng·μL^{-1}) onto the OC surface (see Materials and Methods for experimental details) and recorded their SEIRA spectra using a Fourier-transform infrared (FTIR) spectrometer. Figure 3a–c shows the SEIRA absorption spectra of isofosmoticum-methyl, acetamiprid, and flusilazole at different concentrations, respectively. Correspondingly, Figure 3d–f displays their absorption difference spectra in a colormap format, revealing the spectral response with increasing concentration. All major vibrational peaks within the 1650–750 cm^{-1} fingerprint region are clearly detected, and the absorption intensities exhibit a strong linear correlation with concentration. The OC resonator platform also suppresses Fano-resonance-induced line shape distortions and yields Lorentzian-like absorption profiles, significantly simplifying spectral postprocessing and enhancing robustness. This property provides a reliable spectral basis for downstream AI-based analysis. To further validate the linear relationship between detection signal and target concentration, we extracted intensity curves at representative wavenumbers (Figure 3g–i). Based on the 3σ criterion, the calculated LoDs are 19.6 ng·μL^{-1} (isofosmoticum-methyl), 12.5 ng·μL^{-1} (acetamiprid), and 18.4 ng·μL^{-1} (flusilazole), respectively (see

https://doi.org/10.1021/acsnano.5c20156
ACS Nano 2026, 20, 7730–7742

Supporting Information Figure S8 for background noise). These low detection limits highlight the platform's effectiveness for trace-level pesticide sensing.

We next employed PCA to reduce the dimensionality of the SEIRA spectral data and visualize pesticide classification. Figure 3j presents the absorption spectra of the three pesticides at different concentrations, with each concentration group comprising 50 independent spectra. The full data set was input into the PCA model, and the first three principal components (PC1−PC3) were used to construct a 3D feature space (Figure 3k). In the PCA projection, each color represents a different pesticide: black for isofosmoticum-methyl, green for acetamiprid, and red for flusilazole. The three clusters are clearly separated, demonstrating excellent class separability and validating the OC platform's ability to enhance pesticide-specific vibrational fingerprints for high-accuracy classification. Moreover, within each cluster, spectral samples from different concentrations follow a systematic outward spread from the origin, indicating that concentration variation is primarily manifested in the intensity enhancement of vibrational features, with good linear trends. We further conducted PCA on individual pesticides at different concentrations (Figures 3i and S9, Supporting Information). The resulting clusters corresponding to different concentration gradients were clearly distinguishable, confirming OC resonator's ability to achieve accurate classification across concentration levels. These results demonstrate that the OC resonator platform, owing to its ultrabroadband response, high sensitivity, and inherent immunity to Fano asymmetry, enables multifingerprint enhancement, trace-level pesticide detection, and intelligent quantitative analysis.

Concentration Prediction and Spectral Unmixing of Mixed Pesticides

To further evaluate the potential of the OC resonator platform in identifying components, predicting concentrations, and reconstructing fingerprint spectra in complex pesticide mixtures, we conducted a series of experiments using blends of the three aforementioned pesticides. These molecules exhibit multiple fingerprint absorption peaks within the mid-infrared range of 750−1650 cm^{-1}, with significant spectral overlap and resonance interference. As a result, manual interpretation or traditional linear fitting methods are insufficient for accurate qualitative or quantitative analysis of such mixtures. To validate the OC resonator's capability in separating mixed pesticide samples, we designed a series of mixtures with systematically varied concentration ratios (Figure 4a), covering a wide range of possible combinations. These mixtures were labeled as samples A through V. For each mixture, 50 independent FTIR absorption spectra were recorded, resulting in a large-scale data set comprising approximately 742,500 spectral data points (Figure 4b). This comprehensive data set provided a solid foundation for training subsequent machine learning models.

Each pesticide molecule exhibits unique characteristic vibrational peaks in the mid-infrared region. The OC resonator simultaneously enhances these peaks (Figure S10, Supporting Information), producing spectral signatures that encode both molecular identity and mixture composition. These enriched features provide the necessary information for mixture identification. However, significant peak overlap in mixed spectra makes manual analysis slow and prone to errors. To overcome this, we employed machine learning to automatically extract and interpret the spectral information. Specifically, a SVM classifier was trained on the full spectral data set rather than relying on individual peaks. By learning decision boundaries in the high-dimensional feature space defined by the enhanced vibrational signatures, the SVM could robustly distinguish all mixture classes. As shown in the confusion matrix in Figure 4c, the model achieved 100% classification accuracy across all 22 mixture groups. It is important to emphasize that this high precision arises from the synergistic effect between the rich vibrational fingerprints inherent in pesticide molecules, the broadband and multipeak enhancement provided by the OC resonator, and the AI-based analytical framework.

To further enable precise regression of individual component concentrations in mixed pesticide solutions, we developed MM-DNN model (see Materials and Methods for details). This model was trained using spectral data from Figure 3j and Figure 4b, with the input being the absorption intensity across the fingerprint spectral range and the output being the predicted concentration percentages of the three pesticide components. As shown in Figure 4e, a newly measured set of mixed-solution absorption spectra was used as the test input for the trained MM-DNN model. The predicted results, presented in Figure 4f, demonstrate excellent agreement with the ground truth, achieving a prediction accuracy of 90% (Figure S11, Supporting Information) and a mean absolute error of 0.86 $ng{\cdot}\mu L^{-1}$ (Figure 4g), indicating the model's strong capability in fitting the concentration distribution of complex mixtures.

To further validate the MM-DNN model's spectral unmixing capabilities, we designed a spectrum reconstruction scheme that combines the predicted concentration ratios with reference single-component fingerprint spectra. Taking sample 19 (preset ratio Iso.:Ace.:Flu. = 0:2:1) as an example, we used the concentration weights predicted by the MM-DNN model to reconstruct the mixed absorption spectrum by linearly combining the individual reference spectra. The resulting overlap between the predicted and measured spectra is shown in Figure 4h. Furthermore, to illustrate the model's ability to disentangle component-specific contributions, we multiplied each reference spectrum by its corresponding predicted concentration weight, yielding the decomposed component spectra shown in Figure 4i. Finally, we evaluated the accuracy of spectral reconstruction using the mean squared error (MSE) metric. The reconstructed spectrum of sample V yielded an MSE of 0.02%, indicating high consistency with the experimentally measured spectrum, as well as excellent signal-to-noise ratio and spectral separability. The results in Figure 4 demonstrate that integrating the OC resonator platform with machine learning models can effectively overcome the limitations of conventional methods in the analysis of pesticide mixtures. This hybrid approach significantly enhances both the accuracy and automation level of mixture detection, offering a highly sensitive, intelligent, and scalable solution for pesticide residue monitoring and multicomponent pollutant analysis.

Pesticide Detection on Fruit Skins and in Environmental Water Samples

The development of our experimental platform aims to bridge infrared sensing technology with real-world applications. To evaluate the practical performance of the OC resonator under realistic and complex conditions, we designed two representa-

https://doi.org/10.1021/acsnano.5c20156
ACS Nano 2026, 20, 7730−7742

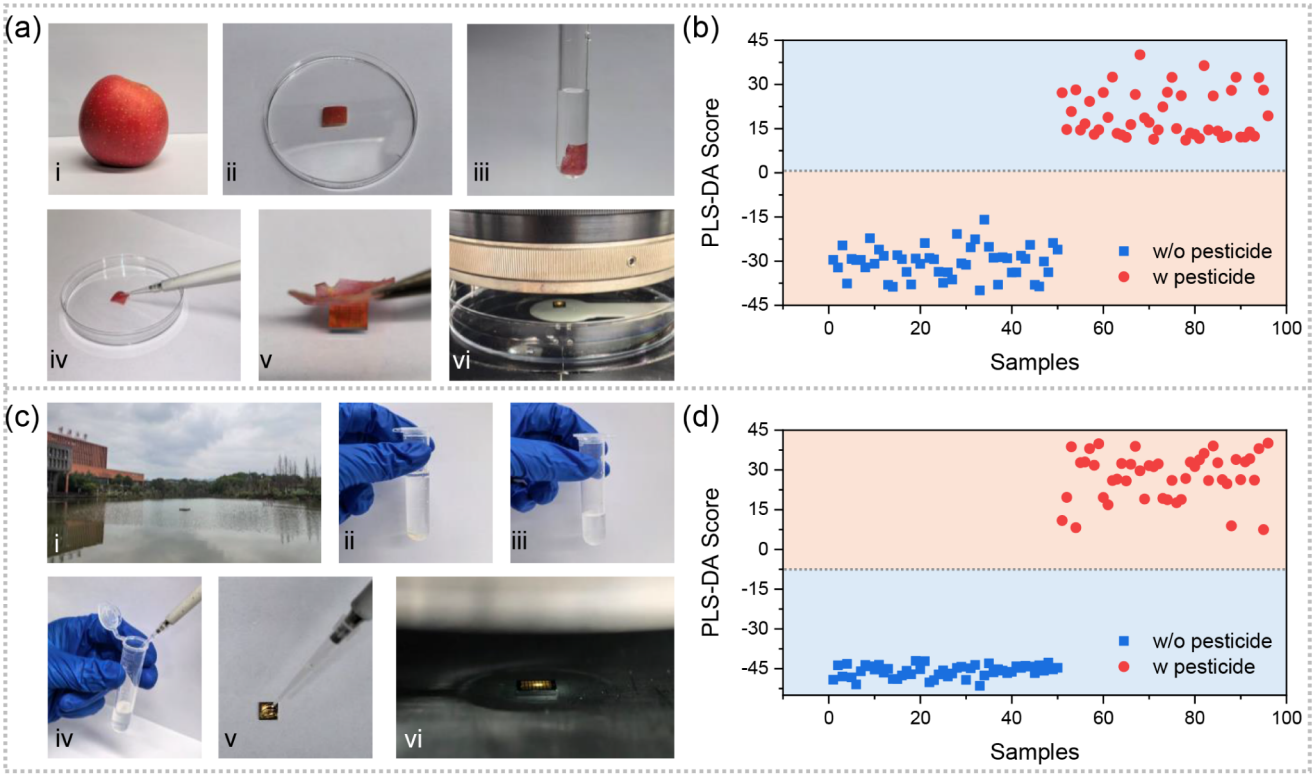

Figure 5. AI-enhanced OC resonator for pesticide detection on fruit peel and in water samples. a) Schematic illustration of the simulated pesticide contamination procedure on fruit peel. b) Classification of measured spectra using a Partial Least Squares Discriminant Analysis (PLS-DA) model for fruit peel samples. c) Schematic illustration of the simulated pesticide contamination procedure in lake water. d) Classification of measured spectra from water samples using the same PLS-DA model.

tive pesticide contamination scenarios: (i) direct pesticide residues on the surface of fruits following spraying, and (ii) environmental pesticide pollution in water bodies caused by leaching into soil and lakes through rainfall. To simulate these scenarios, we selected apple peels and lake water as representative sample types and assessed the detection capability of the OC platform in these real-world contexts.

We first performed a simulation of pesticide residues on fruit skins. Fresh apples (purchased from a local market in Chongqing) were thoroughly rinsed three times with running water to remove surface contaminants. A 1×1 cm^2 square of apple peel was then excised, with the flesh removed and only the skin retained. The samples were sequentially cleaned with methanol, ethanol, and ultrapure water to eliminate any residual impurities and air-dried. A known volume of methyl parathion (MP) standard solution was then drop-cast onto the apple peel to simulate real pesticide exposure. The treated peel was gently affixed onto the OC-MR device and allowed to incubate for 2 min to facilitate molecular adsorption (Figure 5a). FTIR absorption spectra were then recorded from both "blank" samples (no pesticide applied) and "treated" samples (with MP applied) (Figure S12a, Supporting Information). A Partial Least Squares Discriminant Analysis (PLS-DA) model was employed to classify and identify the two sample types. As shown in Figure 5b, blue squares represent untreated apple peels, while red spheres correspond to MP-treated samples. The two groups exhibit clear separation in the PLS-DA feature space, confirming that the OC-AI platform can sensitively detect pesticide molecules on fruit skins.

Next, we evaluated the system's capability for detecting pesticide contamination in water bodies. A 10 mL sample of lake water was randomly collected from Jing Lake on the Huxi Campus of Chongqing University. The water was sequentially processed as follows (Figure 5c): large particulates were first removed via filtration using a 0.22 μm membrane; the filtrate was then centrifuged, and the supernatant was collected. MP standard solution was added to the processed lake water to simulate environmental pesticide contamination. The resulting MP-spiked lake water was drop-cast onto the OC device and allowed air-dry prior to FTIR spectral measurement. Again, we collected FTIR spectra from both the "blank" (uncontaminated) and "treated" (MP-contaminated) lake water samples (Figure S12b, Supporting Information). PLS-DA applied to classify the two groups. As shown in Figure 5d, the model effectively distinguishes between unpolluted (blue) and pesticide-contaminated (red) water samples. The projection distributions in PLS-DA space show clear separation with minimal overlap, indicating that the OC-AI platform also maintains excellent molecular recognition performance under complex aqueous environmental conditions.

CONCLUSIONS

In this study, we developed a broadband OC resonator integrated with AI for multifunctional detection of pesticide molecules. The OC resonator features a high radiative loss rate, enabling ultrabroadband infrared response, high sensitivity, and inherent immunity to Fano asymmetry. The broadband response of the OC resonator effectively covers the characteristic fingerprint region of most pesticide molecules, eliminating the need to tune the resonance frequency for individual analytes and ensuring compatibility across diverse targets. Moreover, the OC resonator exhibits a Lorentzian-like

https://doi.org/10.1021/acsnano.5c20156
ACS Nano 2026, 20, 7730−7742

absorption profile that avoids the spectral distortions commonly introduced by Fano effect in conventional plasmonic structures. This allows the intrinsic molecular vibrational features to appear clearly and symmetrically in the absorption spectra. Such characteristics facilitate simultaneous detection of multiple analytes within a single array and provide a clean spectral foundation ideal for integration with machine learning algorithms for high-dimensional spectral decoding. To validate its performance, we applied the OC platform to detect the infrared fingerprints of four representative pesticide molecules. When combined with machine learning, the system achieved high-precision classification, quantitative concentration prediction, and spectral unmixing of complex mixtures. Experimentally, the proposed system demonstrates broadband operation over the 1650−750 cm^{-1} range, achieves 100% classification accuracy across 22 mixture types, and reaches a minimum LoD down to 12.5 $ng{\cdot}\mu L^{-1}$. We further demonstrated the practical applicability of the OC resonator in simulated real-world contamination scenarios, including pesticide residues on apple peel and in lake water. Using PLS-DA, we achieved clear separation between pesticide-contaminated samples and controls, highlighting the platform's high selectivity and strong interference suppression even in complex environmental backgrounds. Overall, this study emphasizes the synergistic combination of OC resonator and AI-assisted spectral analysis as a new paradigm in SEIRA-based sensing. The integration of AI enhances the platform's ability to process high-dimensional, low-SNR spectral data, enabling reliable molecular identification and concentration quantification in complex mixtures. This innovation not only expands the application scope of SEIRA for pesticide residue detection and environmental monitoring but also provides a general strategy for improving multitarget recognition, broadband enhancement, and robust signal interpretation. The high sensitivity, selectivity, and scalability of this platform suggest promising potential for applications in agricultural safety, environmental risk assessment, and other molecular sensing scenarios under real-world conditions.

MATERIALS AND METHODS

Numerical Simulations

Numerical simulations were performed using a commercial software package (FDTD Solutions ver. 8.19, Lumerical). To improve computational efficiency, periodic boundary conditions were applied along the x and y directions, while perfectly matched layer (PML) boundary conditions were used along the z direction. The structure was illuminated by a normally incident plane wave propagating along the z direction, with the electric field polarized along the x direction. The refractive index of MgF_2 was set to 1.38, and the complex refractive index of gold (Au) was taken from Palik's data. A 3D frequency-domain power monitor was employed to calculate the absorption spectrum, defined as $A = 1 - R - T$, where R and T represent the reflection spectrum and transmission spectrum, respectively. The 10 nm chromium (Cr) adhesion layer was omitted in the simulation for simplification, as its influence on the optical response was negligible.

Device Fabrication

The undercoupled (UC) and overcoupled (OC) resonator devices were fabricated on two 6-in. silicon wafers using standard nanofabrication processes. The silicon wafers were first sequentially cleaned with solvents and dried with nitrogen gas. A 10 nm Cr adhesion layer followed by a 100 nm Au film was deposited by magnetron sputtering to form an optically opaque back reflector. To control the coupling strength of the resonators, a MgF_2 dielectric spacer layer was deposited on the gold-coated substrates by electron-beam evaporation. Two spacer thicknesses were employed: 50 nm for the UC devices and 500 nm for the OC devices. MgF_2 was chosen due to its low optical loss and nearly dispersionless refractive index in the mid-infrared region. The spacer thickness serves as a key design parameter for tuning the balance between radiative and intrinsic loss channels of the resonator. Subsequently, a positive photoresist was spin-coated onto the MgF_2 layer and patterned using stepper lithography. After development, a second metal stack consisting of 10 nm Cr and 100 nm Au was deposited by magnetron sputtering. A liftoff process was then performed to define the final nanoantenna arrays. All fabricated devices were stored in a dry and sealed environment prior to optical characterization.

Experimental Characterization

The morphology of the fabricated devices was characterized using a scanning electron microscope (SEM, Carl Zeiss ΣIGMA 500, Germany). Infrared spectra were collected using a Fourier-transform infrared (FTIR) spectrometer (IR Tracer-100, Shimadzu) coupled with a liquid-nitrogen-cooled mercury cadmium telluride (MCT) infrared microscope (AIM 900, Shimadzu). The microscope was configured with a numerical aperture of 0.4 and a 15× objective lens. A knife-edge aperture was used to restrict the sampling area to a single $100 \times 100\ \mu m^2$ antenna array. The reflectance spectrum of a gold mirror was used as background reference. All spectra were collected in the mid-infrared region from 750 to 4000 cm^{-1}. The FTIR parameters were set as follows: mirror scanning speed of 40 kHz, spectral resolution of 4 cm^{-1}, and 16 scans per measurement averaged to obtain the final spectrum.

Sample Preparation

Poly(methyl methacrylate) (PMMA) was used as a molecular probe to evaluate the surface-enhanced infrared absorption (SEIRA) performance of the OC resonator. A 1 wt % PMMA solution (molecular weight 495 kDa) in anisole was spin-coated onto the device surface at 4000 rpm for 60 s, followed by thermal baking at 180 °C for 3 min to form a uniform thin molecular layer.

For quantitative pesticide detection experiments, individual pesticide solutions, including isofosmoticum-methyl, acetamiprid, and flusilazole, were prepared in methanol with concentrations ranging from 25 to 500 $ng{\cdot}\mu L^{-1}$. The corresponding complex permittivity data are provided in Figure S13 and Tables S1−S3 of the Supporting Information. To simulate real-world residue detection scenarios, methyl parathion (MP) was selected as a representative organophosphorus pesticide and applied at a concentration of 100 $ng{\cdot}\mu L^{-1}$ onto apple peel and lake water samples without additional chemical treatment.

A single OC resonator array was used for SEIRA enhancement verification, single-pesticide quantification, mixture analysis, and real-sample evaluation to eliminate device-to-device variations. For each measurement, 2 μL of solution was drop-cast onto the OC resonator surface using a calibrated micropipette (Research Plus, Eppendorf) and allowed to dry naturally under ambient conditions for 10 min prior to spectral acquisition. After each measurement, the device was sequentially rinsed in methanol and deionized water for 5 min each to remove residual analytes, followed by nitrogen drying. To ensure complete removal of surface-bound molecules and maintain reproducibility, the OC resonator was further cleaned using oxygen plasma treatment for 5 min before subsequent measurements.

Data Processing and Machine Learning

Spectral preprocessing, parameter fitting, vibrational signal extraction, postprocessing, and principal component analysis (PCA) were performed using Origin software (OriginLab Corporation, USA). PCA was applied to visualize spectral variance and assess intrinsic clustering behavior prior to classification. The support vector machine (SVM) classifier was implemented in Python 3.11.5 using the scikit-learn 1.2.2 library. As SVM is inherently a binary classifier, multiclass recognition tasks were decomposed into multiple binary classification problems to distinguish between different molecules or mixture types.

https://doi.org/10.1021/acsnano.5c20156
ACS Nano 2026, 20, 7730−7742

The data set was split with 80% used for training and 20% for testing, and a linear kernel function was employed for classification.

For concentration prediction, a multimodal deep neural network (MM-DNN) model was developed using Python 3.11.5 and scikit-learn. The network was constructed with Keras as a sequential model consisting of an input layer, three hidden layers, and an output layer. The input layer contained 675 neurons corresponding to the number of data points in each spectrum. Each hidden layer had 128 neurons activated by the ReLU function. The output layer comprised three neurons representing predicted component concentrations and used a linear activation function. Model training was conducted using the Adam optimizer and mean squared error (MSE) as the loss function, with evaluation metrics including mean absolute error (MAE) and prediction accuracy.

Partial Least Squares Discriminant Analysis (PLS-DA) was applied to FTIR spectral data to classify pesticide-treated and untreated samples. The data set was randomly split into a training set (20%) and a test set (80%). A PLS regression model with five latent variables was trained, and classification was based on a 0.5 threshold applied to predicted continuous values. The first latent variable (Component 1) scores for test samples were visualized and exported for further analysis.

Ethics Statement

This study did not involve human participants, animal experiments, or clinical samples. All experiments were performed using commercially available pesticide standards in accordance with institutional laboratory safety guidelines. Therefore, ethical approval was not required.

■ ASSOCIATED CONTENT

Data Availability Statement

The data generated for this study has been provided in the main text and Supporting Information. Additional information can be provided upon reasonable request.

Supporting Information

The Supporting Information is available free of charge at https://pubs.acs.org/doi/10.1021/acsnano.5c20156.

Section S1 describes the temporal coupled mode theory; Figures S1−S13 present the effects of loss and detuning on sensitivity, sensitivity comparisons, numerical simulations of loss and frequency responses, device characterization, fitting of experimental spectra, noise measurements, principal component analysis, sensing signal analysis, results of the multimodal deep neural network, measured spectra, and the complex permittivity spectra of the samples; Table S1 summarizes the Drude−Lorentz model parameters of the samples (PDF)

■ AUTHOR INFORMATION

Corresponding Authors

Xiaojing Mu − *Key Laboratory of Optoelectronic Technology & Systems of Ministry of Education, Chongqing University, Chongqing 400044, China;* orcid.org/0000-0003-2024-2595; Email: mxjacj@cqu.edu.cn

Chengkuo Lee − *Department of Electrical and Computer Engineering, National University of Singapore, Singapore 117583, Singapore; Center for Intelligent Sensors and MEMS, National University of Singapore, Singapore 117608, Singapore;* orcid.org/0000-0002-8886-3649; Email: elelc@nus.edu.sg

Authors

Dongxiao Li − *Department of Electrical and Computer Engineering, National University of Singapore, Singapore 117583, Singapore; Center for Intelligent Sensors and MEMS, National University of Singapore, Singapore 117608, Singapore*

Ziwei Chen − *Key Laboratory of Optoelectronic Technology & Systems of Ministry of Education, Chongqing University, Chongqing 400044, China*

Xueyuan Wu − *Key Laboratory of Optoelectronic Technology & Systems of Ministry of Education, Chongqing University, Chongqing 400044, China*

Tao Liu − *Key Laboratory of Optoelectronic Technology & Systems of Ministry of Education, Chongqing University, Chongqing 400044, China*

Guozhi Zhang − *Department of Electrical and Electronic Engineering, Hubei University of Technology, Wuhan 430068, China*

Complete contact information is available at: https://pubs.acs.org/10.1021/acsnano.5c20156

Author Contributions

#D.L. and Z.C. contributed equally to this work. D.L., Z.C., X.M., and C.L. conceived the project. D.L. performed the numerical simulations, theoretical analysis, device fabrication, processing of the simulation and experimental data, and wrote the manuscript. Z.C. carried out numerical simulations, sensing experiments, data analysis, and drafted the manuscript. X.W. assisted with the sensing experiments. T.L. and G.Z. discussed the experimental results. X.M. and C.L. supervised the project. All authors contributed to revising the manuscript and approved the final version.

Notes

The authors declare no competing financial interest.

■ ACKNOWLEDGMENTS

This research was supported by the General Program of National Natural Science Foundation of China (NSFC No. 52075061), the Key Program of the National Natural Science Foundation of China (NSFC No. U22B2089), the National Key Research and Development Program of China (Grant Nos. 2022YFB3205400 and 2021YFB2012100), the Fundamental Research Funds for the Central Universities (Grant No. 2024CDJGF-005), the Science Fund for Distinguished Young Scholars of Chongqing (Grant No. CSTB2022 NSCQJQX0006), and the National Foreign Experts Program (S20250239). This work was also supported by the Agency for Science, Technology and Research (A*STAR), Singapore, under Grant Nos. M22H1b0110, M24W1NS005, and M23M5a0069.

■ REFERENCES

(1) Song, R.; Zhang, Y.; Lu, P.; Wu, J.; Li, Q. X.; Song, B. Status and perspective on green pesticide utilizations and food security. *Annu Rev Food Sci Technol.* **2024**, *15* (1), 473−493.

(2) Yang, M.; Wang, Y.; Yang, G.; Wang, Y.; Liu, F.; Chen, C. A review of cumulative risk assessment of multiple pesticide residues in food: Current status, approaches and future perspectives. *Trends Food Sci. Technol.* **2024**, *144*, 104340.

(3) Froger, C.; Jolivet, C.; Budzinski, H.; Pierdet, M.; Caria, G.; Saby, N. P.; Arrouays, D.; Bispo, A. Pesticide residues in French soils:

Occurrence, risks, and persistence. *Environ. Sci. Technol.* **2023**, *57* (20), 7818−7827.
(4) Navarro, I.; De la Torre, A.; Sanz, P.; Abrantes, N.; Campos, I.; Alaoui, A.; Christ, F.; Alcon, F.; Contreras, J.; Glavan, M.; et al. Assessing pesticide residues occurrence and risks in water systems: A Pan-European and Argentina perspective. *Water Res.* **2024**, *254*, 121419.
(5) Li, W.; Xin, S.; Deng, W.; Wang, B.; Liu, X.; Yuan, Y.; Wang, S. Occurrence, spatiotemporal distribution patterns,partitioning and risk assessments of multiple pesticide residues in typical estuarine water environments in eastern China. *Water Res.* **2023**, *245*, 120570.
(6) Pico, Y.; Alfarhan, A. H.; Barcelo, D. How recent innovations in gas chromatography-mass spectrometry have improved pesticide residue determination: An alternative technique to be in your radar. *TrAC, Trends Anal. Chem.* **2020**, *122*, 115720.
(7) Brandi, J.; Siragusa, G.; Robotti, E.; Marengo, E.; Cecconi, D. Analysis of veterinary drugs and pesticides in food using liquid chromatography-mass spectrometry. *TrAC, Trends Anal. Chem.* **2024**, *179*, 117888.
(8) Song, X.-Y.; Shi, Y.-P.; Chen, J. Carbon nanotubes-reinforced hollow fibre solid-phase microextraction coupled with high performance liquid chromatography for the determination of carbamate pesticides in apples. *Food Chem.* **2013**, *139* (1−4), 246−252.
(9) Aly, N.; Mosallam, E.; Ahmed, N.; El-Gendy, K. Development and validation of a novel enzyme-linked immunosorbent assay for monitoring ethylene thiourea in soil and vegetable samples. *Food Chem.* **2020**, *325*, 126931.
(10) Karoui, R.; Downey, G.; Blecker, C. Mid-infrared spectroscopy coupled with chemometrics: A tool for the analysis of intact food systems and the exploration of their molecular structure− quality relationships− a review. *Chem. Rev.* **2010**, *110* (10), 6144−6168.
(11) Neubrech, F.; Huck, C.; Weber, K.; Pucci, A.; Giessen, H. Surface-Enhanced Infrared Spectroscopy Using Resonant Nanoantennas. *Chem. Rev.* **2017**, *117* (7), 5110−5145.
(12) Li, D.; Wu, X.; Chen, Z.; Liu, T.; Mu, X. Surface-enhanced spectroscopy technology based on metamaterials. *Microsyst. Nanoeng.* **2025**, *11* (1), 60.
(13) Zhou, H.; Li, D.; Lv, Q.; Lee, C. Integrative plasmonics: Optical multi-effects and acousto-electric-thermal fusion for biosensing, energy conversion, and photonic circuits. *Chem. Soc. Rev.* **2025**, *54*, 5342−5432.
(14) Kozuch, J.; Ataka, K.; Heberle, J. Surface-enhanced infrared absorption spectroscopy. *Nat. Rev. Methods Primers* **2023**, *3* (1), 70.
(15) Li, D.; Xu, C.; Xie, J.; Lee, C. Research Progress in Surface-Enhanced Infrared Absorption Spectroscopy: From Performance Optimization, Sensing Applications, to System Integration. *Nanomaterials* **2023**, *13* (16), 2377.
(16) Altug, H.; Oh, S. H.; Maier, S. A.; Homola, J. Advances and applications of nanophotonic biosensors. *Nat. Nanotechnol.* **2022**, *17* (1), 5−16.
(17) Li, D.; Zhou, H.; Hui, X.; He, X.; Mu, X. Plasmonic Biosensor Augmented by a Genetic Algorithm for Ultra-Rapid, Label-Free, and Multi-Functional Detection of COVID-19. *Anal. Chem.* **2021**, *93* (27), 9437−9444.
(18) Hui, X.; Yang, C.; Li, D.; He, X.; Huang, H.; Zhou, H.; Chen, M.; Lee, C.; Mu, X. Infrared Plasmonic Biosensor with Tetrahedral DNA Nanostructure as Carriers for Label-Free and Ultrasensitive Detection of miR-155. *Adv. Sci.* **2021**, *8* (16), No. e2100583.
(19) Zhou, H.; Ren, Z.; Li, D.; Xu, C.; Mu, X.; Lee, C. Dynamic construction of refractive index-dependent vibrations using surface plasmon-phonon polaritons. *Nat. Commun.* **2023**, *14* (1), 7316.
(20) Niemann, R.; Mueller, N. S.; Wasserroth, S.; Lu, G.; Wolf, M.; Caldwell, J. D.; Paarmann, A. Spectroscopic and Interferometric Sum-Frequency Imaging of Strongly Coupled Phonon Polaritons in SiC Metasurfaces. *Adv. Mater.* **2024**, *36* (33), No. e2312507.
(21) Zhou, H.; Li, D.; Ren, Z.; Xu, C.; Wang, L.-F.; Lee, C. Surface plasmons-phonons for mid-infrared hyperspectral imaging. *Sci. Adv.* **2024**, *10* (22), No. eado3179.
(22) Rosas, S.; Schoeller, K. A.; Chang, E.; Mei, H.; Kats, M. A.; Eliceiri, K. W.; Zhao, X.; Yesilkoy, F. Metasurface-Enhanced Mid-Infrared Spectrochemical Imaging of Tissues. *Adv. Mater.* **2023**, *35* (28), No. e2301208.
(23) Li, D.; Zhou, H.; Hui, X.; He, X.; Huang, H.; Zhang, J.; Mu, X.; Lee, C.; Yang, Y. Multifunctional Chemical Sensing Platform Based on Dual-Resonant Infrared Plasmonic Perfect Absorber for On-Chip Detection of Poly(ethyl cyanoacrylate). *Adv. Sci.* **2021**, *8* (20), 2101879.
(24) Chen, Z.; Li, D.; Zhou, H.; Liu, T.; Mu, X. A hybrid graphene metamaterial absorber for enhanced modulation and molecular fingerprint retrieval. *Nanoscale* **2023**, *15* (34), 14100−14108.
(25) Tittl, A.; Leitis, A.; Liu, M.; Yesilkoy, F.; Choi, D. Y.; Neshev, D. N.; Kivshar, Y. S.; Altug, H. Imaging-based molecular barcoding with pixelated dielectric metasurfaces. *Science* **2018**, *360* (6393), 1105−1109.
(26) Richter, F. U.; Sinev, I.; Zhou, S.; Leitis, A.; Oh, S. -H.; Tseng, M. L.; Kivshar, Y.; Altug, H. Gradient High-Q Dielectric Metasurfaces for Broadband Sensing and Control of Vibrational Light-Matter Coupling. *Adv. Mater.* **2024**, *36* (25), No. e2314279.
(27) Aigner, A.; Weber, T.; Wester, A.; Maier, S. A.; Tittl, A. Continuous spectral and coupling-strength encoding with dual-gradient metasurfaces. *Nat. Nanotechnol.* **2024**, *19*, 1804−1812.
(28) Aigner, A.; Tittl, A.; Wang, J.; Weber, T.; Kivshar, Y.; Maier, S. A.; Ren, H. Plasmonic bound states in the continuum to tailor light-matter coupling. *Sci. Adv.* **2022**, *8* (49), No. eadd4816.
(29) Zhou, H.; Hui, X.; Li, D.; Hu, D.; Chen, X.; He, X.; Gao, L.; Huang, H.; Lee, C.; Mu, X. Metal−Organic Framework-Surface-Enhanced Infrared Absorption Platform Enables Simultaneous On-Chip Sensing of Greenhouse Gases. *Adv. Sci.* **2020**, *7* (20), 2001173.
(30) Ren, Z.; Zhang, Z.; Wei, J.; Dong, B.; Lee, C. Wavelength-multiplexed hook nanoantennas for machine learning enabled mid-infrared spectroscopy. *Nat. Commun.* **2022**, *13* (1), 3859.
(31) Rodrigo, D.; Tittl, A.; Ait-Bouziad, N.; John-Herpin, A.; Limaj, O.; Kelly, C.; Yoo, D.; Wittenberg, N. J.; Oh, S. H.; Lashuel, H. A.; et al. Resolving molecule-specific information in dynamic lipid membrane processes with multi-resonant infrared metasurfaces. *Nat. Commun.* **2018**, *9* (1), 2160.
(32) Rodrigo, D.; Limaj, O.; Janner, D.; Etezadi, D.; Garcia de Abajo, F. J.; Pruneri, V.; Altug, H. Mid-infrared plasmonic biosensing with graphene. *Science* **2015**, *349* (6244), 165−168.
(33) Hu, H.; Yang, X.; Zhai, F.; Hu, D.; Liu, R.; Liu, K.; Sun, Z.; Dai, Q. Far-field nanoscale infrared spectroscopy of vibrational fingerprints of molecules with graphene plasmons. *Nat. Commun.* **2016**, *7*, 12334.
(34) Leitis, A.; Tittl, A.; Liu, M.; Lee, B. H.; Gu, M. B.; Kivshar, Y. S.; Altug, H. Angle-multiplexed all-dielectric metasurfaces for broadband molecular fingerprint retrieval. *Sci. Adv.* **2019**, *5* (5), No. eaaw2871.
(35) Li, D.; Zhou, H.; Chen, Z.; Ren, Z.; Xu, C.; He, X.; Liu, T.; Chen, X.; Huang, H.; Lee, C.; et al. Ultrasensitive Molecular Fingerprint Retrieval Using Strongly Detuned Overcoupled Plasmonic Nanoantennas. *Adv. Mater.* **2023**, *35* (32), No. e2301787.
(36) Li, D.; Zhou, H.; Ren, Z.; Xu, C.; Lee, C. Tailoring Light−Matter Interactions in Overcoupled Resonator for Biomolecule Recognition and Detection. *Nano Micro Lett.* **2025**, *17* (1), 10.
(37) Zhou, H.; Li, D.; Ren, Z.; Mu, X.; Lee, C. Loss-induced phase transition in mid-infrared plasmonic metamaterials for ultrasensitive vibrational spectroscopy. *InfoMater* **2022**, *4* (12), No. e12349.
(38) Adato, R.; Artar, A.; Erramilli, S.; Altug, H. Engineered absorption enhancement and induced transparency in coupled molecular and plasmonic resonator systems. *Nano Lett.* **2013**, *13* (6), 2584−2591.
(39) Paggi, L.; Fabas, A.; El Ouazzani, H.; Hugonin, J. P.; Fayard, N.; Bardou, N.; Dupuis, C.; Greffet, J. J.; Bouchon, P. Over-coupled resonator for broadband surface enhanced infrared absorption (SEIRA). *Nat. Commun.* **2023**, *14* (1), 4814.
(40) da Silveira Petruci, J. F.; da Silva Sousa, D.; Mizaikoff, B. Advanced Mid-Infrared Sensors for Molecular Analysis. *Anal. Chem.* **2025**, *97* (13), 6871−6890.

https://doi.org/10.1021/acsnano.5c20156
ACS Nano 2026, 20, 7730−7742

(41) John-Herpin, A.; Kavungal, D.; von Mucke, L.; Altug, H. Infrared Metasurface Augmented by Deep Learning for Monitoring Dynamics between All Major Classes of Biomolecules. *Adv. Mater.* **2021**, *33* (14), 2006054.
(42) Zhou, H.; Xu, L.; Ren, Z.; Zhu, J.; Lee, C. Machine learning-augmented surface-enhanced spectroscopy toward next-generation molecular diagnostics. *Nanoscale Adv.* **2023**, *5* (3), 538−570.
(43) Kavungal, D.; Magalhães, P.; Kumar, S. T.; Kolla, R.; Lashuel, H. A.; Altug, H. Artificial intelligence−coupled plasmonic infrared sensor for detection of structural protein biomarkers in neurodegenerative diseases. *Sci. Adv.* **2023**, *9* (28), No. eadg9644.
(44) Tittl, A.; John-Herpin, A.; Leitis, A.; Arvelo, E. R.; Altug, H. Metasurface-Based Molecular Biosensing Aided by Artificial Intelligence. *Angew. Chem. Int. Ed.* **2019**, *58* (42), 14810−14822.
(45) Guo, X.; Zhang, Z.; Ren, Z.; Li, D.; Xu, C.; Wang, L.; Liu, W.; Zhuge, Y.; Zhou, G.; Lee, C. Advances in Intelligent Nano-Micro-Scale Sensors and Actuators: Moving toward Self-Sustained Edge AI Microsystems. *Adv. Mater.* **2025**, *37* (50), No. e10417.
(46) Zhou, H.; Li, D.; Lee, C. Technology landscape review of in-sensor photonic intelligence: From optical sensors to smart devices. *AI Sens.* **2025**, *1* (1), 5.
(47) Lechenet, M.; Dessaint, F.; Py, G.; Makowski, D.; Munier-Jolain, N. Reducing pesticide use while preserving crop productivity and profitability on arable farms. *Nat. Plants* **2017**, *3* (3), 17008.
(48) Yadav, S. K. Pesticide applications-threat to ecosystems. *J. Hum. Ecol.* **2010**, *32* (1), 37−45.
(49) Maggi, F.; Tang, F. H.; Tubiello, F. Agricultural pesticide land budget and river discharge to oceans. *Nature* **2023**, *620* (7976), 1013−1017.
(50) Liu, X.; Starr, T.; Starr, A. F.; Padilla, W. J. Infrared spatial and frequency selective metamaterial with near-unity absorbance. *Phys. Rev. Lett.* **2010**, *104* (20), 207403.
(51) Liu, N.; Mesch, M.; Weiss, T.; Hentschel, M.; Giessen, H. Infrared Perfect Absorber and Its Application As Plasmonic Sensor. *Nano Lett.* **2010**, *10* (7), 2342−2348.
(52) Haus, H. A.; Haus, H. A. N x N coupled waveguide switch. *Opt. Lett.* **1984**, *9* (10), 466−467.
(53) Yi, J.; You, E. M.; Ding, S. Y.; Tian, Z. Q. Unveiling the molecule-plasmon interactions in surface-enhanced infrared absorption spectroscopy. *Natl. Sci. Rev.* **2020**, *7* (7), 1228−1238.

https://doi.org/10.1021/acsnano.5c20156
ACS Nano 2026, 20, 7730−7742